Applied Materials Today 21 (2020) 100789

Contents lists available at ScienceDirect

Applied Materials Today

journal homepage: www.elsevier.com/locate/apmt

Fingerprints of relaxor ferroelectrics: Characteristic hierarchical domain configurations and quantitative performances

Jihong Bian[a,*], Pan Xue[c], Ren Zhu[d], Lei Wang[a], Bian Yang[a], Tao Li[e], Qingyuan Hu[f], Lvkang Shen[f], Jianwei Wang[a], Guanghao Lu[a,*], Yaodong Yang[b,*]

[a] Frontier Institute of Science and Technology, State Key Laboratory for Mechanical Behavior of Materials, Xi'an Jiaotong University, Xi'an 710054, China
[b] School of Mechanical and Automotive Engineering, Qilu University of Technology (Shandong Academy of Sciences), Jinan, 250353, China
[c] The State Key Laboratory of ASIC and System, Fudan University, Shanghai 201203, China
[d] Oxford Instruments, No. 461 Hongcao Road, Shanghai 200233, China
[e] Center for Spintronics and Quantum Systems, State Key Laboratory for Mechanical Behavior of Materials, Department of Materials Science and Engineering, Xi'an Jiaotong University, Xi'an, Shaanxi 710049, China
[f] Electronic Materials Research Laboratory, Key Laboratory of the Ministry of Education & International Center for Dielectric Research, School of Microelectronics, Xi'an Jiaotong University, Xi'an 710049, China

ARTICLE INFO

Article history:
Received 7 May 2020
Revised 29 July 2020
Accepted 7 August 2020

Keywords:
Domain
Ferroelectrics
Scanning probe microscopy
Quantitative performance
Single crystal

ABSTRACT

Ferroelectrics' structure-property relationships are of guiding significance in high-performance material designing and usually clarified from the aspect of symmetries, which is arduous and costly. On the principle of convenience, here, the concept that domains can provide a brandnew nondestructive and fast way for this relationship clarification is demonstrated. Utilizing scanning probe microscopy, quantitative original local elastic/piezoelectric/ferroelectric performances of various characteristic domain configurations are directly investigated in relaxor ferroelectric $Pb(Mg_{1/3}Nb_{2/3})O_3$-$PbTiO_3$ single crystals. Among them, the polygonal lamellar domains with coexistence of straight c, a and c/a walls in the at-morphotropic phase boundary composition, own high surface effective Young's modulus (average values close to 160 GPa), strong original average local piezoresponse (8.5 pm) and effective longitudinal piezoelectric response (d_{33}, 14 pm V^{-1}), together with ease of electrical switching. Low free energy barrier and strong piezoelectric anisotropy contribute intrinsically to these better functionalities. Higher and easier domain wall motion, larger ratio of c^+/c^- domains, and larger depolarization and elastic energies stemmed from larger domain width/size act as extrinsic factors. These results help to understand relaxor ferroelectrics comprehensively and provide a reference of domain-based structure selection for better material design.

1. Introduction

Ferroelectrics have a wide application in industry as actuators, transducers, memories, and ultrasonic/optical-electric/energy harvesting devices [1,2], because of their excellent dielectric/piezoelectric/photoelectric performances. Among them, relaxor ferroelectrics, e.g., $(1-x\%)Pb(Mg_{1/3}Nb_{2/3})O_3$-$x\%PbTiO_3$ (PMN-x%PT), attract much more attention than others by virtue of ultrahigh electromechanical and optoelectric [3] capabilities. For instance, the macroscopic longitudinal piezoelectric response (d_{33}) of PMN-PT single crystals (e.g., > 2500 pC N^{-1}) around morphotropic phase boundary (MPB) is four times larger than that of the best doped $PbZr_{0.48}Ti_{0.52}O_3$ ceramics in value of ~500 pC N^{-1} [4,5]. Debate on the origin of these attracting performances in relaxor-PT based solid solutions has never stopped over the past two decades, due to the complexity in distinguishing symmetries accurately via combination of various diffraction techniques [6-9], such as reciprocal space map, synchrotron radiation, neutron diffuse scattering and Raman scattering. Moreover, these revelation is arduous, time-consuming and costly.

Apart from the atomic arrangement related symmetries, domains are crucial to ferroelectrics' basic structure-property relationship understanding and performance tailoring. Domains, i.e., areas having the same polarization direction, are one of the essential, distinct but vital microstructures in ferroelectrics. Domain formation bounds up with structural symmetries resulted from atoms' arrangement, long range order (LRO) and vibration. With the capability to be easily reconfigured by external electric or elastic field, domains can affect ferroelectrics' functionalities notably, especially for nanomaterials. For instance, polar nanoregions

* Corresponding authors.
E-mail addresses: bjh.90@stu.xjtu.edu.cn (J. Bian), guanghao.lu@mail.xjtu.edu.cn (G. Lu), yaodongy@xjtu.edu.cn (Y. Yang).

https://doi.org/10.1016/j.apmt.2020.100789
2352-9407/

(PNRs) [4,10], one unique kind of microstructures in relaxor ferroelectrics, may formed due to pinning by local strong enough random field [6]. They can facilitate polarization rotation thanks to their ease of switching abilities by external stimuli, and thus contribute largely (e.g., 50%–80%) to the aforementioned novel longitudinal and shear electromechanical properties [4,10]. Despite the fact that ferroelectric domains with longer range ordered are still different from PNRs in short range order (SRO), these inspiring findings highlight the significance of microstructures to properties. Besides, domains and domain walls are found to have intriguing phenomena basically different from their parent materials like wall conductivity [11] and vortex domains [12], triggering evolution on applications in nanoelectronic devices. Furthermore, macroscopic performances (e.g., di-, piezo-, opto- and pyro-electric performances) of relaxor ferroelectrics can be greatly further enhanced and tailored via domain engineering [3,5,13], through manipulation of domain patterns, width or sizes, amount and motion of domain walls.

Various kinds of microscopies make it convenient to visualize domain patterns, including polarized optical microscopy (POM) [14,15], transmission electron microscopy [16,17], scanning electron microscopy [18], piezoresponse force microscopy (PFM) [6,19,20]. Quite plenty of works have reported domain configurations in relaxor-PT solid solutions, however, several key issues on structure-property relationship clarification from the aspect of domains are not stated clearly. Firstly, the lateral component of polarization vector affects in-plane electromechanical capabilities greatly but is seldom characterized. Moreover, for the previous out-of-plane domain configuration observation, uniform conclusion can hardly be drawn due to the divergences in the reported case-by-case specimens, aside from the complexity in domains themselves originated from doping of relaxors (e.g., PMN) into ferroelectrics (e.g., PT). For instance, multiple states coexisted complex domains at MPB in the (001) PMN-PT single crystals at room temperature via POM were observed [14]. But elsewhere, in the near-MPB-composition of PMN-PT by the same technique, fine crosshatched domains in rhombohedral (R) symmetry were found [21]. In contrast, by PFM, a domain hierarchy on length scales from 40 nm to 0.1 mm presents in PMN-PT single crystals [15]. Nanodomains with opposite polarization orientation embedded on the micro-sized domains can be seen [15], indicating the coexistence of polar clusters within ferroelectric domains [6]. Secondly, despite its indispensable significance in clarifying the domain structure-property relationships, direct evidence between these configurations and in-situ properties of domains has seldom been provided in the simple binary [17,22] relaxor-PT systems, ascribed to difficulties in combination of the conventional macroscopic property detection techniques with the aforementioned microscopies. Not to mention those complex cases in the ternary [23-25] and even quaternary [26] systems. Without better solutions and direct experimental proofs, domain patterns are usually merely thought and believed to be related and contribute to relaxor ferroelectrics' macroscopic capabilities, acquired from macroscopic permittivity-temperature relationships, hysteresis [polarization versus electric field (P-E)] loops and strain-electric field curves [7,27]. To be more rigorous, direct dielectric/ferroelectric/elastic domain properties contributing to macro-performances are needed urgently. Thirdly, comprehensive and direct relationships between configurations and in-situ original properties of domains in relaxor ferroelectrics are far in lack, especially experimentally. The recent rapid development of scanning probe microscopy (SPM) facilitates the possibility of visualizing domain configurations and characterizing their local multifunctionality conveniently on mesoscale. However, quantitative performances by nondestructive and fast testing methods in relaxor ferroelectrics still remain unknown. For instance, in the rare reported studies for elastic property characterization, the commonly used nano-indentation [28], force curve and three-point bending [29] methods have slow test rate and sampling heterogeneity. More importantly, the excessive applied forces by these means result in damage to specimens' surfaces such as protrusion [28], dent, or even cracks [29], which are not desirable and should be avoided especially for nanomaterials/devices. On the other hand, for piezoelectric/ferroelectric performance measurement, the reported after-normalization [22,30] piezoresponses without cantilever calibration are incomparable from case to case, making it confusing to distinguish the best corresponding material. Without cantilever calibration of inverse optical lever sensitivity and spring constant, the detected responses usually include a tip-sample-dependent equipment magnification and thus cannot reflect the intrinsic properties of the materials themselves. This magnification is quite common in commercial PFM utilizing a piezo ceramic to generate cantilever's vibration, and should be eliminated in quantitative analyses.

In this work, we clarify relationships between various typical vertical and lateral domain configurations and their original in-situ quantitative local elastic/piezoelectric/ferroelectric performances, in the simple binary relaxor ferroelectric PMN-x%PT single crystals mainly by SPM. Direct evidence of better domain properties in the at-MPB composition is given. Great variation in local effective piezoresponse and effective d_{33} values without/with cantilever calibration is revealed. Extrinsic and intrinsic factors are discussed for explanation of these performance differences. These investigations help draw a round picture of domain structures in the relaxor ferroelectric, provide a domain perspective for structure-property relationship clarifying and offer a reference of domain-based structure selection for better material design.

2. Materials and methods

Commercial (100)-oriented unpoled relaxor ferroelectric PMN-x%PT (x = 24, 32, 40) single crystals (MTI Group, Hefei, China) of R, monoclinic (M) and tetragonal (T) symmetries, respectively, were utilized as specimens. All the samples were cut into 5 mm × 5 mm × 0.2 mm, with upper and bottom surfaces polished to optical surface finish.

Domain structures on microscale were visualized by POM (LV100POL, Nikon eclipse, Japan) in transmission mode. Configurations and in-situ properties of surface domains on mesoscale were characterized by SPM (Cypher S, Asylum research, USA) in various modes. Vector PFM (VPFM) was utilized for vertical and lateral domain configuration visualization, while DART PFM which had utilized the dual-frequency resonance tracking technique already was for vertical ones observation. Conductive Ti/Pt-coated silicon cantilevers (AC240TM, Olympus; spring constant = 2 N m^{-1}, tip radius = 28 ± 10 nm) were used in both VPFM and DART PFM modes. In VPFM characterization, the vertical applied ac drive amplitude was 0.8 V, and the corresponding drive frequency was 200–240 kHz; the lateral drive amplitude was 2 V, and the corresponding drive frequency was 600–680 kHz. In DART PFM characterization, the applied ac driving amplitude was 0.8 V, and the drive frequency was 200–240 kHz. The test frequency was chosen a little aside the contact resonance peak. The quality (Q) factor of the contact resonance peak was different according to different locations, in a typical range from 25 to 268 here.

Sizes and ratio of c^+ and c^- domains were statistically analyzed by the software ImageJ. Domains of c^+ and c^- in the specimens were firstly identified and zoned according to different color contrast in PFM phase and low response in PFM amplitude. In principle, each domain can be considered to be in mathematical convex shape. Areas in concave shape, which can be considered as the combination of multiple smaller convex domains, should be divided into several convex shapes inside the region. These spe-

cific secondary partition is not present in detail. After partitioning, the area around the edge of each domain partition is the single domain area, the longest distance between any two points is the length of the single domain, and the shortest distance between any two points is the width of the single domain. The area, length and width were then measured by ImageJ using the function "Measure". For each domain, these parameters were measured 10 times and averaged, as their area/length/width. Then, all these area/length/width of a single c^+ or c^- domain was averaged and analyzed statistically to acquire the area/length/width of a single c^+/c^- domain in each specimen.

Domain switching evolution and retention experiments were carried out by DART PFM and litho PFM. DART PFM (ac voltage = 0.8 V, resonant frequency = 200–240 kHz) observed in-situ pristine and switching-after domain patterns. Conductive Ti/Pt-coated silicon cantilevers (AC240TM, Olympus; spring constant = 2 N m^{-1}, tip radius = 28 ± 10 nm) were used. Various external electric dc voltages with magnitude from 5 V to 40 V were applied to the tip via litho PFM for writing the pristine domains with certain patterns locally.

Local surface elastic properties were characterized by amplitude modulation-frequency modulation (AM-FM). To reduce the influence of probe choice, two kinds of non-conductive silicon cantilevers with different tip materials were used: i) with high-density diamond-like carbon tips (Biosphere B20-NCH, Nanotools; spring constant = 40 N m^{-1}, tip radius = 20 ± 5 nm) and ii) with silicon tips (AC160TS-R3, Olympus; spring constant = 26 N m^{-1}, tip radius = 9 ± 2 nm). Using blunt tips eliminates the tip-sample contact area effect, by which deeper regions would exhibit larger effective Young's modulus. The deflection sensitivity, spring constant and tip radius of cantilevers were calibrated before measurement of the specimens, utilizing a piece of common silicon single crystal with a known elastic modulus (160 GPa) as the reference sample for cantilever calibration. This calibration affects the absolute value of effective Young's modulus but has little effect on that of effective stiffness. The absolute value of effective stiffness varies with different tips but does not affect the relative value relation on compositions in the specimens. The acquired AM-FM phase less than 60°, and clear frequency responses guarantee the good quality and reliability of our AM-FM results.

Local electromechanical responses were detected by DART switching spectroscopy PFM (SS-PFM). Conductive Ti/Pt-coated silicon cantilevers (AC240TM, Olympus; spring constant = 2 N m^{-1}, tip radius = 28 ± 10 nm) were used. Data sets of local SS-PFM amplitude butterfly curves and phase switching hysteresis loops in the off-field state were acquired at each point of the 50 × 50 grids on the 5 μm × 5 μm regions in PMN-24%PT and PMN-32%PT and of the 20 × 20 grids on the 500 nm × 500 nm region in PMN-40%PT by SS-PFM in mapping mode. The latter is with much higher resolution. For all the specimens, the maximum applied dc voltage was 40 V, the drive ac amplitude to the tip was 0.8 V, and the scanning direction was from down to up. The drive frequency was 203.7 kHz for PMN-24%PT, 290.9 kHz for PMN-32%PT and 235.8 kHz for PMN-40%PT. The Q factor of contact resonance is related to the cantilever and sample local stiffness, in value of tens to hundreds, being different at each point of the SS-PFM testing grids. For the uncalibrated data processing, all the data from the above 2500 or 400 groups of loops were utilized, using the default inverse optical lever sensitivity (InvOLS, especially the amplitude InvOLS which can be short for "Amp InvOLS") being 109 nm V^{-1} and default spring constant in value of 1.00 nN nm^{-1}, including the magnification effect of the contact resonance. In-situ spatial distribution maps of positive switching voltage (V_+), negative switching voltage (V_-), coercive voltage (V_c) and imprint voltage (V_i) were extracted. In extraction of coercive voltage by the Asylum software, the coercive voltage was considered as the voltage where the PFM amplitude of the SS-PFM loops was the lowest. Consequently, the degradation of the tip may cause a decrease in PFM amplitude of the entire SS-PFM loop, but would not change the corresponding voltage related to the lowest amplitude. In other words, the degradation of the tip may result in a decrease in PFM amplitude, but should not influence the measurement of coercive voltage directly. Thus the degradation of the tip would have little effect on our results which could be omitted. For quantitative analyses, before each DART SS-PFM mapping measurement, after finishing the tip focus and sample focus procedures, cantilever's parameters such as Amp InvOLS, spring constant and so on were firstly calibrated via the "GetReal" function of the Asylum Software. For PMN-24%PT, the Amp InvOLS was 71.19 nm V^{-1}, and spring constant was 1.48 nN nm^{-1}. For PMN-32%PT, the Amp InvOLS was 59.71 nm V^{-1}, and spring constant was 3.33 nN nm^{-1}. For PMN-40%PT, the Amp InvOLS was 64.15 nm V^{-1}, and spring constant was 1.87 nN nm^{-1}. Then, hysteresis loops at each point of the 50 × 50 or 20 × 20 grids were acquired using the "SHO (simple harmonic oscillator) fitting" function to exclude the magnification effect of Q factor of the contact resonance. Not all the data could be well SHO fitted. Abandoning those bad-fitted or unsaturated results, only about 100–200 groups of data remained from the calibrated 2500 (of PMN-24%PT and PMN-32%PT) or 400 (of PMN-40%PT) data sets for the with-calibration data processing.

Local piezo response and effective longitudinal piezoelectric response (or named "effective d_{33}") were defined and calculated by two formulas with different variables, namely, Piezoresponse (pm) = Amplitude (pm) × cos (Phase) and Effective d_{33} (pm V^{-1}) = Amplitude (pm)/Applied ac voltage (V), respectively. After averaging the corresponding data above, SS-PFM amplitude butterfly loops, phase switching loops, local hysteresis loops (piezo response) and effective longitudinal piezoelectric response loops in the three specimens without/with cantilever calibration were plotted. All these loops are a little deviated from their zero points due to the existence of built-in electric field. Hence, we used Average Piezoresponse = ($|Piezoresponse_{max}|+|Piezoresponse_{min}|$)/2, Average Effective d_{33} = |the maximum d_{33}|-| the minimum d_{33}|, Average SS-PFM amplitude = Average Effective d_{33} × Detected ac Voltage as the piezo response, effective d_{33} and average SS-PFM amplitude, respectively, of each single crystal.

The scan rates of PFM scanning, litho switching, SS-PFM map testing and AM-FM scanning were set at 3.91 Hz, 1 Hz, 2.44 Hz and 2 Hz, respectively. As these samples have high phase transition temperature, thermal fluctuation has no effect on the results here, but induces thermal drift. To minimize the thermal drift, three hours were taken before measurements, and all the scan rates are sufficiently fast. Fine-tuning the scanning regions using characteristic features from the images was carried out to track the thermal drift and ensure in-situ scanning regions.

3. Results and discussion

3.1. Hierarchical domain configurations

According to phase diagram [9,16,31] of PMN-x%PT (an illustration shown in Fig. S1) at room temperature, the off-MPB compositions, PMN-24%PT and PMN-40%PT, have R and T symmetry, respectively; while the MPB composition, PMN-32%PT, is in a M phase [16,31,32]. Domain configurations on microscale and mesoscale in PMN-x%PT single crystals are shown in Fig. 1. By POM, spindle-like domains form 90° patterns in all specimens. With the content of PT increasing, domains in length of 10–80 μm become thinner and shorter at MPB, with some even vanish at several spots; and then self-assembled into longer stripes forming a cross-hatched pattern. Different from the similar look of these microscale stripe-like patterns, characteristic mesoscale vertical (do-

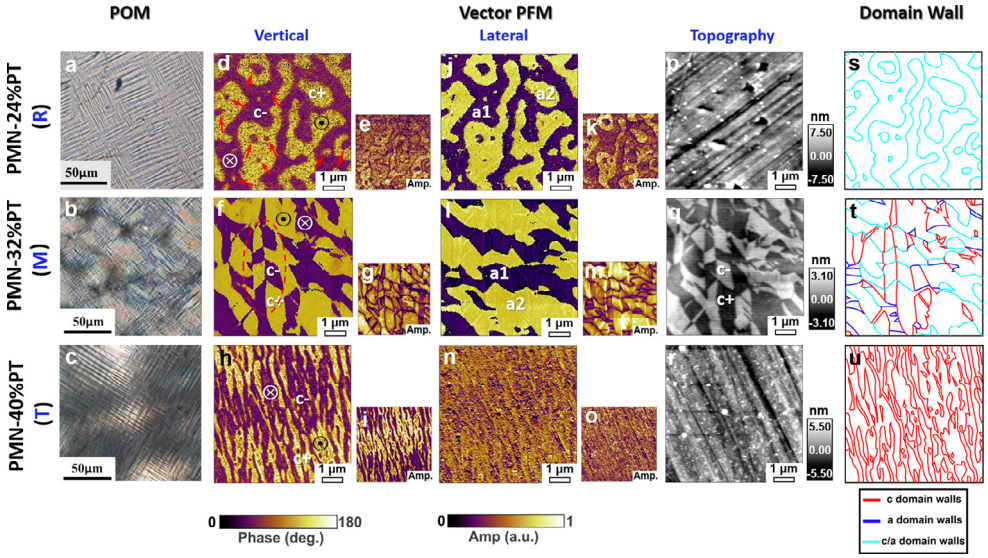

Fig. 1. Hierarchical domain configurations in (100)-oriented unpoled PMN-24%PT, PMN-32%PT and PMN-40%PT single crystals. Stripe domains on microscale by POM in (a) PMN-24%PT, (b) PMN-32%PT and (c) PMN-40%PT. Vertical PFM phase and amplitude, lateral PFM phase and amplitude, and surface topography signals on 7 μm × 7 μm by VPFM are shown in (d,e), (j,k) and (p), respectively, for PMN-24%PT; in (f,g), (l,m) and (q), respectively, for PMN-32%PT; and in (h,i), (n,o), and (r), respectively, for PMN-40%PT. Schematics of domain walls in (s) PMN-24%PT, (t) PMN-32%PT and (u) PMN-40%PT.

main with out-of-plane polarization, namely, c domain) and lateral (domain with in-plane polarization, namely, a domain) domain configurations by VPFM in the three crystals vary greatly from each other (Fig. 1d-r). Schematics of domain wall kinds are illustrated in Fig. 1s-u. Amplitude responses depict electromechanical magnitude, while phase signals illustrate polarization orientation. With increasing contents of Ti^{4+} across MPB, labyrinthine domains with curved c/a walls in PMN-24%PT, alter to polygonal lamellar ones with coexistence of relatively straight c, a and c/a walls in PMN-32%PT, then to ribbon-like slim ones with only c walls in small curvature in PMN-40%PT. Antiparallel nanodomains are embedded in the micron-domains in PMN-24%PT (labelled by the red arrows in Fig. 1d) and PMN-40%PT. Twin domains exist in PMN-32%PT (red ellipse in Fig. 1f). Vertical and lateral domains in (100)-oriented rhombohedral PMN-24%PT have the same configuration, since all the eight equivalent spontaneous polarization vectors contribute equally to these responses. In PMN-32%PT, lamellar lateral domains whose length is throughout the whole field of vision, are larger sized and in obviously different configurations compared with those of the vertical ones. The lateral responses in PMN-40%PT are interfered by crosstalk of its strong vertical signals and hence, only c domains exist. Fig. S2 presents distinct vertical domain configurations on larger scanning regions. Purple vertical domains have down-ward polarization (c^- domains), and the yellow ones have up-ward polarization (c^+ domains). Recognition of c^+/c^- domains can be proved by electrical switching results below. Intriguingly, in PMN-32%PT, vertical domains can be distinguished in majority from surface topography: c^+ domains are probably related to deeper regions in topography. All the samples only have out-of-plane crystal axes determined. The in-plane crystal axes are not determined so that we cannot tell the domain wall orientation direction specifically.

3.2. Responses to local external electric field

Polarization responses to the various tip-applied external dc electric voltages from 0 V to ±40 V are present in Fig. 2a,e and Fig. S3, within a certain pattern (Fig. 2b). Under proper positive dc fields, c^+ domains reverse into c^- ones through polarization rotation; and c^- can switch into c^+ by proper negative voltages (Fig. 2c). After the double-box poling processes, there was no change in the surface morphology, thus only one topography image of each single crystal was present in Fig. S3a,i,q. Fig. 2d illustrates the visualized vertical domain reversal and domain wall motion (emergence or disappearance). The pristine polygonal lamellar domains in PMN-32%PT are the easiest to be electrically switched, with partial and complete switching voltages in magnitude as low as 10 V and 14 V, respectively. Labyrinthine domains in PMN-24%PT are the most difficult to be reversed, suggested by their total switching threshold voltage of ±18 V. Retention results of reversed domains by ±30 V indicate that after electrical reversal for 24 h, all the switched domains still exist (Fig. S4). To be honest, it is quite difficult to determine the real depth of these poled domains. The coercive field of PMN-PT single crystal is low, with typical value of less than 500 V mm^{-1} (0.5 V μm^{-1}) [9], or ~2.3 kV cm^{-1} (0.23 V μm^{-1}) [13]. Usually, dc fields with values two to three times larger than the coercive field can switch the sample throughout the thickness direction completely [13]. Then, the dc voltage of 40 V is not sufficient to switch domains down to the bottom. Thus, possibly, these poled domains were just formed in the vicinity of the top surface of the samples. All specimens' average piezoelectric responses are effectively increased after switching (Fig. 2e), in accordance with the enhancement of piezoelectricity/ferroelectricity by poling on macro scale [13,33]. Among all the crystals, both the pristine and switched domains of PMN-32%PT own the strongest piezoelectricity, revealed by average amplitude of 80 pm and 100 pm, respectively.

3.3. Quantitative analyses of local performances

3.3.1. Local surface elastic properties

In these chemically homogeneous PMN-x%PT single crystals, surface elastic properties by AM-FM using a high-density diamond-like carbon tip are present in Fig. 3 and Fig. S5. Results by a silicon tip are provided in Fig. S6.

All the samples have smooth surfaces, despite the existence of scratches caused by polishing in PMN-24%PT and PMN-40%PT, and the surface fluctuation related to c^+/c^- domains in PMN-32%PT. In both cases using the two kinds of probes, on average, the effective Young's modulus of PMN-24%PT is the lowest (90.5 GPa), while

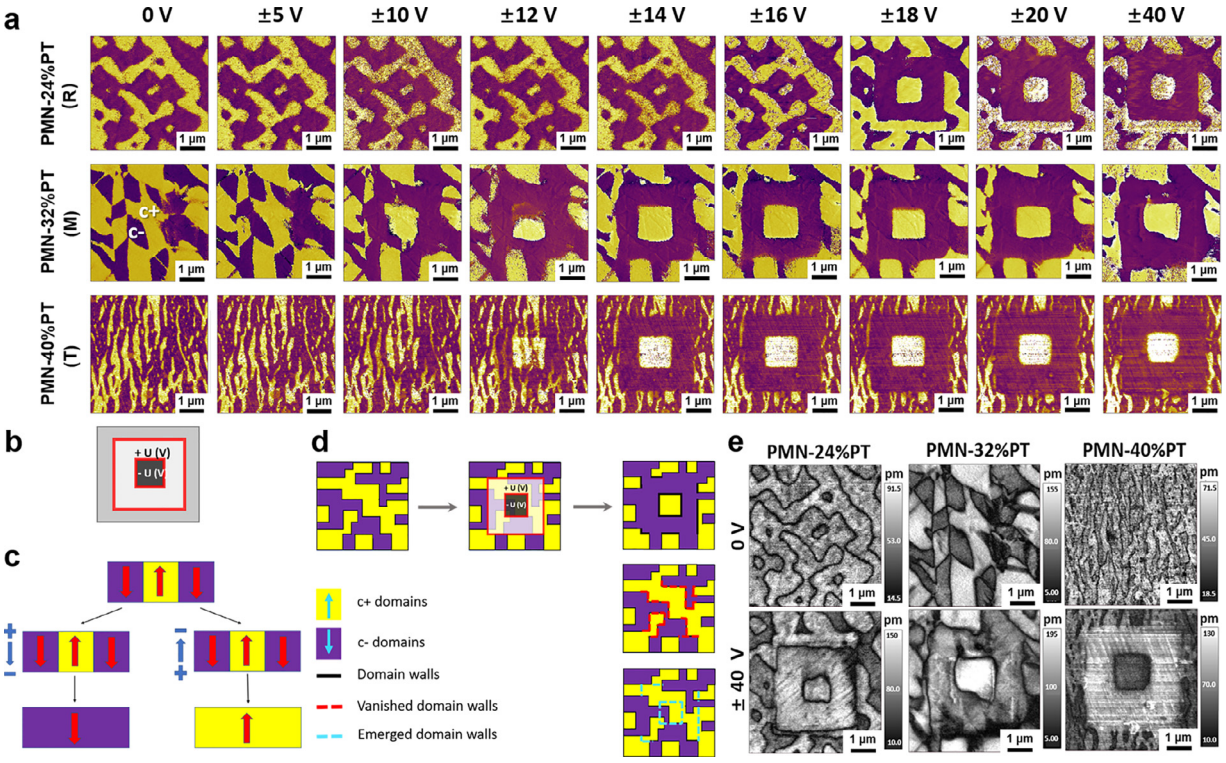

Fig. 2. (a) PFM phase of in-situ domain evolution on 5 μm × 5 μm by dc electrical switching from 0 V to ±40 V in PMN-24%PT, PMN-32%PT and PMN-40%PT. (b) The schematic of dc voltages' application. Positive voltages were applied on the central 3 μm × 3 μm (in white) and negative ones with the same magnitude on the central 1 μm × 1 μm (in black). The whole pristine region is 5 μm × 5 μm (in gray). (c) Schematics of c domain switching processes and determination of c^+/c^- by external dc electric field. (d) Schematics of domain reversal and domain wall motion during switching. (e) PFM amplitude changes of pristine and electrically switched domains by dc ±40 V without cantilever calibration.

those in PMN-32%PT (117–158 GPa) and PMN-40%PT (116/144 GPa) are comparable to that of the silicon single crystal (160 GPa). The effective stiffness changes on compositions have a similar trend. The wide range variations in the average values of effective Young's modulus in PMN-32%PT and PMN-40%PT are attributed to divergences in local regions and the chosen tips. In PMN-32%PT, it can be seen that c^+ and c^- domains have almost equal effective Young's modulus and effective stiffness (Fig. 3d-l and Fig. S6a-c). Consequently, the value variation of elastic property among the three local regions in PMN-32%PT is not ascribed to the amount difference of c^+/c^- domains, but may relate with surface defects such as domain walls and oxygen vacancies.

3.3.2. Local piezoelectricity and ferroelectricity

Vertical domains and their corresponding in-situ spatial distribution maps of V_+, V_-, V_c and V_i by SS-PFM in PMN-x%PT are present in Fig. 4. A correlation between these characteristic electrical-switching voltage parameters and domain structures can be seen in all the specimens. Characteristic voltages of c^+ domains are smaller than those of c^- domains. Table S1 lists the average switching voltages extracted from the distribution maps and those calculated by $V_c = (|V_+|+|V_-|)/2$ and $V_i = (|V_+|-|V_-|)/2$. Despite a small deviation in values, the direct-read and calculated V_c and V_i are close to each other in a similar relative magnitude trend. The results show that PMN-32%PT has the smallest average coercive voltage V_c (11.75 V from calculated result and 15 V from direct-read result) and the largest average imprint voltage V_i (8.75 V from calculated result and 5.5 V from direct-read result) among the three specimens, revealing its relative ease of electrical domain switching and higher magnitude of imprint which originates from internal electric field and leads to a shift in the ferroelectric hysteresis loop along the field axis [34,35]. This higher magnitude of imprint may be related to a higher concentration of defect dipoles such as oxygen vacancies in this monoclinic MPB-composition, which can be aligned and stabilize the domain configuration along polarization direction during dc poling [34]. These results are in accordance with those observed responses to external electric field.

Quantitative average local electromechanical loops in the three specimens with/without calibration are plotted in Fig. 5 and Fig. S7.

The square SS-PFM local hysteresis loops (Fig. 5c and Fig. S7c) are similar to those P-E loops characterized by macroscopic measurements [36,37]. The shape of local hysteresis in relaxors is controlled by local properties (e.g., local relaxation time spectrum), while in ferroelectrics it is defined by nonlocal polarization wall dynamics [38]. It should be noted that possible electrostatic field effect or the interaction between the cantilever and the sample surface directly affect the PFM amplitude and thus affect the quantitative analyses of piezoelectricity. The electrostatic field effect would influence the phase difference. If the phase difference is around 180°, then the electrostatic effect could be ignored. In our results, both in PFM signals and SS-PFM loops we can see that the phase difference is around 180°. This experimental fact thus excludes the contribution of the electrostatic field effect. Usually, to apply a dc voltage to the probe or sample surface may help compensate the surface potential of the sample which may cause the electrostatic field effect. But in our experiments, the surface potentials of all the samples were too small to result in large electrostatic field effect. As a result, no external dc voltage was needed.

Table S2 and Table 1 record the maximum/minimum and average piezoresponse and effective d_{33} in the three specimens ex-

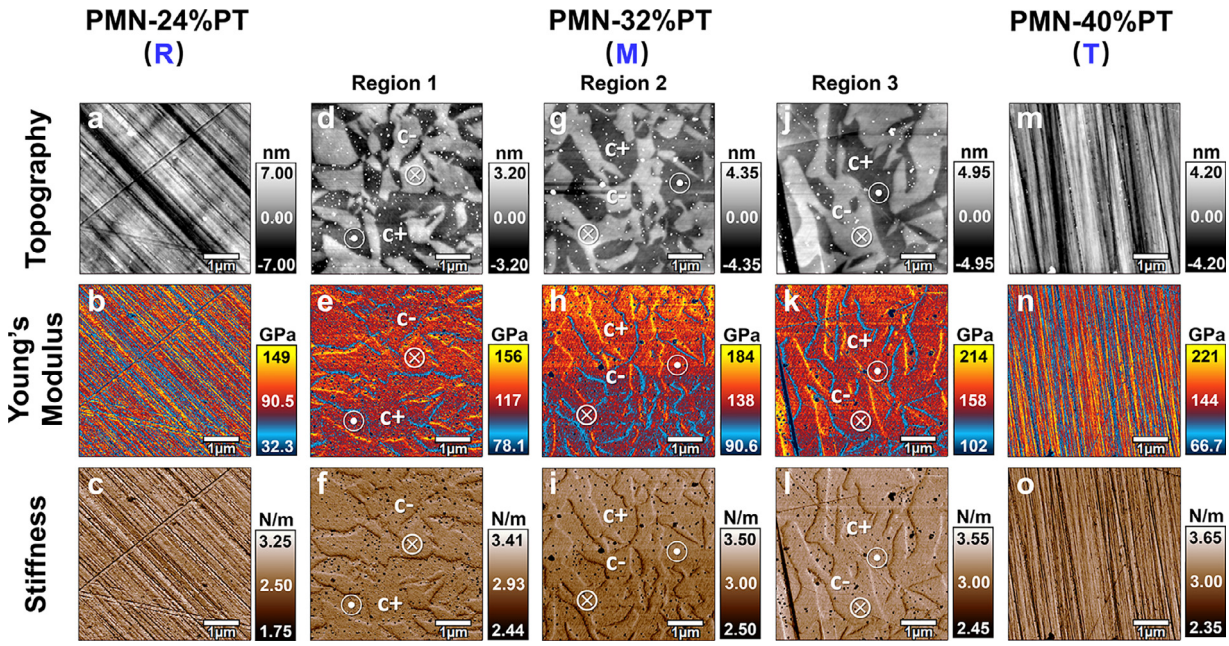

Fig. 3. Topography, in-situ Young's modulus and stiffness images in (a-c) PMN-24%PT, (d-l) PMN-32%PT and (m-o) PMN-40%PT via AM-FM using a high-density diamond-like carbon tip (Biosphere B20-NCH, Nanotools; non-conductive silicon cantilever; spring constant = 40 N m^{-1}, tip radius = 20 ± 5 nm). For PMN-32%PT, results of three regions are presented: (d-f) region 1, (g-i) region 2 and (j-l) region 3.

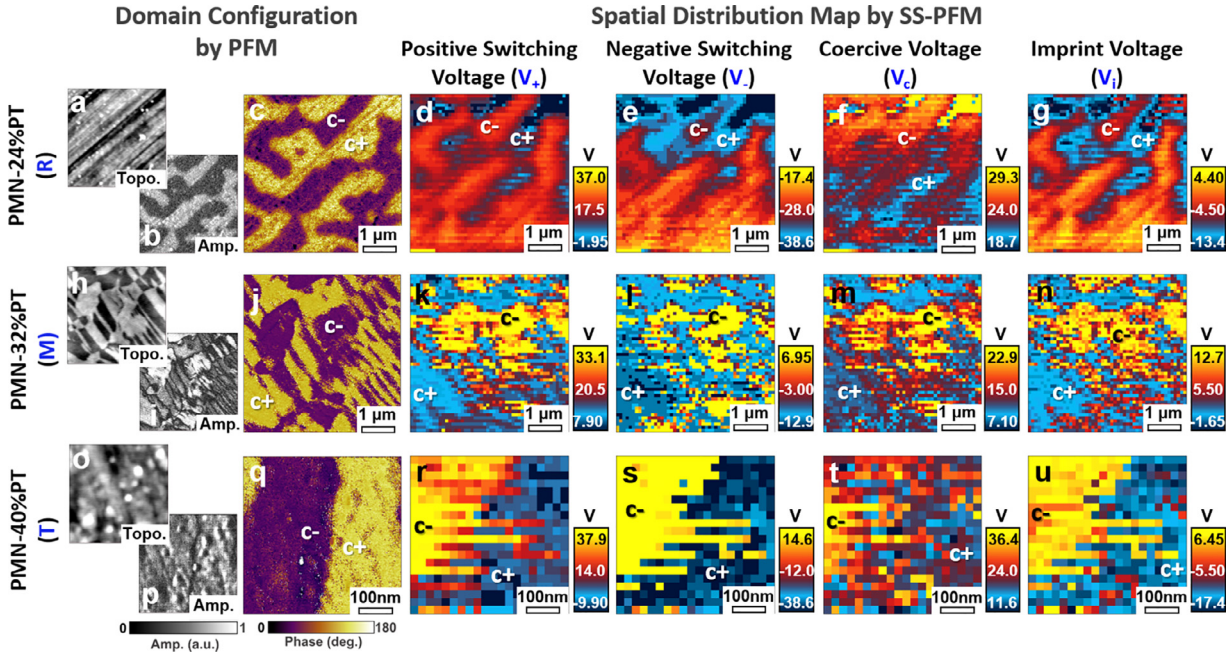

Fig. 4. Domain configurations and their corresponding in-situ spatial distribution maps of characteristic electrical-switching voltage parameters, i.e., V_+, V_-, V_c and V_i by SS-PFM in (a-g) PMN-24%PT, (h-n) PMN-32%PT and (o-u) PMN-40%PT. Vertical domain configurations by PFM in (a-c) PMN-24%PT, (h-j) PMN-32%PT and (o-q) PMN-40%PT. PFM topography and amplitude images are in black and white and labeled with "Topo." and "Amp.", respectively. Distribution maps acquired from the local switching curves in (d-g) PMN-24%PT (50 × 50 pixels within 5 μm × 5 μm), (k-n) PMN-32%PT (50 × 50 pixels within 5 μm × 5 μm) and (r-u) PMN-40%PT (20 × 20 pixels within 500 nm × 500 nm).

Table 1
The average piezoresponse, effective d_{33} and amplitude without/with cantilever calibration (using default/calibrated Amp InvOLS and spring constant, without/with SHO fitting) in PMN-24%PT, PMN-32%PT and PMN-40%PT, extracted from local hysteresis loops and effective d_{33} versus voltage loops.

	Average Piezoresponse(pm)		Average Effective d_{33}(pm V^{-1})		Average Amplitude(pm)	
	Without calibration	With calibration	Without calibration	With calibration	Without calibration	With calibration
PMN-24%PT	117.5	6.75	150	9.1	120	7.28
PMN-32%PT	180	8.5	245	14	196	11.2
PMN-40%PT	120	7.45	165	10.1	132	8.08

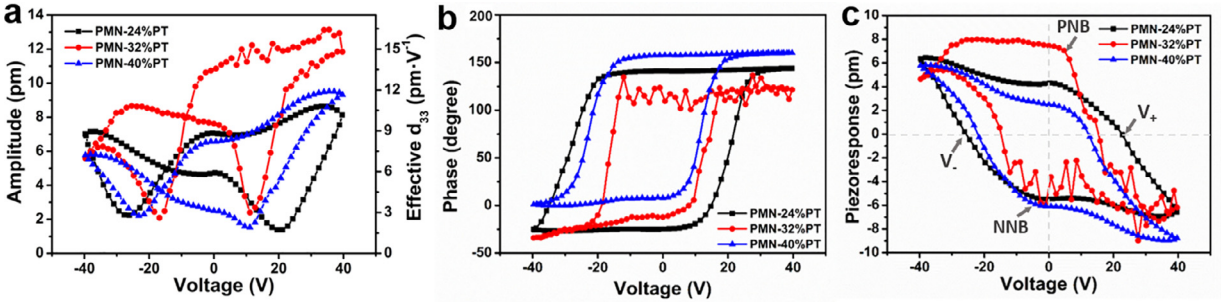

Fig. 5. Quantitative average local electromechanical properties in PMN-24%PT, PMN-32%PT and PMN-40%PT single crystals, processed averagely using the 100–200 data sets from the spatial distribution maps with cantilever calibration over 5 μm × 5 μm (for PMN-24%PT and PMN-32%PT) or 500 nm × 500 nm (for PMN-40%PT). (a) SS-PFM amplitude butterfly loops and effective longitudinal piezoelectric response (d_{33}) versus voltage loops; (b) SS-PFM phase switching hysteresis loops; (c) Local hysteresis loops.

Table 2
PNB, NNB, stability gap, built-in electric potential, V_+, V-, V_c and V_i in the PMN-x%PT (x = 24, 32, 40) single crystals from the original local hysteresis loops (with cantilever calibration, excluding the magnification effect of contact resonance) by SS-PFM.

	PNB (V)	NNB (V)	V_+(V)	V-(V)	Stability Gap(V)	Built-in Electric Potential(V)	Coercive Voltage(V)	Imprint Voltage(V)
PMN-24%PT	4.2	−5.8	22.5	−25.9	10	−1.6	24.2	−1.7
PMN-32%PT	4.9	−7.1	15.2	−14.9	12	−2.2	15.05	0.15
PMN-40%PT	6.7	−6.2	12.1	−22.2	12.9	0.5	17.15	−5.05

tracted from these local loops. Firstly, it can be seen that domains in PMN-32%PT at MPB own the strongest local piezoelectric/ferroelectric response (the strongest piezo response in value of 8.5 pm and largest effective d_{33} of 14 pm V^{-1} with calibration), while those in the PMN-24%PT (piezo response of 6.75 pm and effective d_{33} of 9.1 pm V^{-1}) and PMN-40%PT (piezo response of 7.45 pm and effective d_{33} of 10.1 pm V^{-1}) located off MPB have comparable magnitudes. This trend is further supported by those observed in Fig. 2e, value divergences of which come mainly from method differences. PFM amplitudes reflect intrinsic contribution from lattice strain to the piezoelectricity, while SS-PFM loops contain domain wall motion effect induced by electrically switching. More reversed domains and higher level of domain wall motion occur here by the SS-PFM mapping, contribute greatly to the larger piezoresponses. Secondly, a huge data value decrease between the cases without and with cantilever calibration is revealed, suggesting the significance of cantilever calibration process on the quantitative analyses of piezoelectricity. For instance, with cantilever calibration, the average effective d_{33} of PMN-32%PT decreases from 245 pm V^{-1} to 14 pm V^{-1}, the latter of which represents the original piezoelectric magnitudes. The hysteresis results without cantilever calibration could be easily mistaken for samples' piezoelectricity/ferroelectricity determination. However, in this process using default Amp InvOLS of 109 nm V^{-1} and default spring constant of 1.00 nN nm^{-1} without SHO fitting, the contributions of magnification from the equipment, contact resonance or many details of testing procedures (e.g., location of cantilever focus, the specific detected region, etc.) are usually included. For quantitative analyses, cantilever calibration is required.

Thirdly, positive nucleation bias (PNB), negative nucleation bias (NNB), stability gap (defined by PNB-NNB), built-in electric potential (defined by PNB+NNB), V_+ and V-, V_c and V_i are extracted from the original local hysteresis loops (Table 2). V_c and V_i are close to and in a similar tendency with those in Table S1. The positive values of stability gap indicate the ferroelectric property, and the increase in this parameter with Ti^{4+} increasing suggest the increased stability of the bias-switched states in the crystals. [38] The built-in electric field, related with local defects such as frozen electric random fields, accounts for the deviation from zero point in the P-E loops, [38] exhibiting as the aforementioned imprint phenomena.

The values of imprint voltage in the three single crystals from Table 2 and Table S1 show a deviation, resulted from different sample sizes and sources of test data. The average imprint voltages listed in Table S1 were acquired from the SS-PFM imprint voltage spatial distribution map (Fig. 4g,n,u), using SS-PFM local switching curves without cantilever calibration. The sample size is large: 2500 groups of data sets for PMN-24%PT and PMN-32%PT (50 × 50 pixels on the 5 μm × 5 μm regions) and 400 groups of loops for PMN-40%PT (20 × 20 pixels on the 500 nm × 500 nm region). As a contrast, the imprint voltages in Table 2 were taken from the original local hysteresis loops with cantilever calibration by SS-PFM, which represent intrinsic properties of the single crystals. But the sample size is much smaller compared with those in Table S1: only 100–200 groups of well-SHO-fitted hysteresis data sets were used for data processing and plotting. Those bad fitted data were abandoned. Both of these values are reliable. The ones in Table S1 reflect the properties of local regions directly with a larger sample size.

3.4. Discussion

3.4.1. Domain formation

Domain formation is ascribed to i) the balance between random field and ferroelectric interaction of nanoclusters, and ii) gradient-driven morphological transition. Labyrinthine domain configurations can be considered as a feature in the (100)-oriented rhombohedral relaxor-PT single crystals with low PT content, as observed here in PMN-24%PT and reported in other systems like $Pb(Mg_{1/3}Nb_{2/3})O_3$-$PbZrO_3$-$PbTiO_3$ [25] and $Pb(In_{1/2}Nb_{1/2})O_3$-$PbZrO_3$-$Pb(Mg_{1/3}Nb_{2/3})O_3$-$PbTiO_3$ [26]. These configurations are formed by the disappearance or mergence of the SRO nano-sized polar clusters and their aggregations, which is attributed to the stronger influence of random field over the ferroelectric interaction. Particularly, the strong-enough local random field in some regions, pinning the PNR and their aggregations in the opposite direction from their surrounding ferroelectric microdomains, gives rise to the occurrence of nano antiparallel domains embedded inside the micron-domains (Fig. 1b). Noting that PMN is a pure relaxor and PT is a pure ferroelectric, the introduction of Ti^{4+} cations tends to increase the size of polar clusters via increasing the off-center displacement, thereby strengthening the interaction

between dipolar moments leading to long-range symmetry breaking [6,14]. Thus we infer that it changes from SRO in dominant to coexistence of SRO and LRO, and then to LRO in dominant with the content of Ti^{4+} increasing in PMN-x%PT solid solution. The random field originates from built-in charge disorder and decreases with increasing substitution of Ti^{4+} cation [6,19] in relaxor-PT systems. Consequently, in compositions with more PT content, ascribed to the weaker effect of random field over the ferroelectric interaction, domains self-organize into lamellar or ribbon-like patterns according to their macroscopic symmetries to minimize elastic energy, as the cases in PMN-32%PT and PMN-40%PT.

From another aspect, it is predicted theoretically by the Landau-Ginzburg-Devonshire (LGD) approach that the labyrinthine domain configurations, which have the minimal energy between the gradient-correlation energy and electrostatic energy, could lead to the gradient-induced morphological transition [39]. As the gradient coefficient g_{44} increases, the labyrinthine-like feature turns to ribbon-like one, which can be verified experimentally here by the PFM vertical domain configuration transformations from PMN-24%PT to PMN-40%PT. Thus, the vertical domain patterns in PMN-24%PT and PMN-40%PT are induced by this gradient-driven transition as well.

Intriguingly, vertical domains in PMN-32%PT can be distinguished in majority from their surface topographies. In the PMN-24%PT with R symmetry and PMN-40%PT with T symmetry, the c domains do not show any relation to their topography images here. However, the analogous phenomena as observed in PMN-32%PT have been reported in other relaxor-PT single crystals with various symmetries by different researchers, e.g., $Pb(Zn_{1/3}Nb_{2/3})O_3$-$PbTiO_3$ (PZN-PT) with R or T phases [29, 40] and $Pb(In_{1/2}Nb_{1/2})O_3$-$Pb(Mg_{1/3}Nb_{2/3})O_3$-$PbTiO_3$ (PIN-PMN-PT) located close to MPB but slightly on the R side [24]. All of these indicate that these phenomena are not unique but common. Thus, in AM-FM, the elastic properties of c^+/c^- domains were just determined from PMN-32%PT. These phenomena of c domain-topography relation can be attributed to the mechanochemical polishing effect [24,40], which was believed to be related with the mechanical differences (e.g., hardness) between the head and tail parts of the domains. It is quite intriguing and unexpected that head and tail parts of domains are possibly to have property differences, for instance, response to mechanical load [41] and spatial current distribution [42]. Besides, this phenomenon may suggest the sensitivity of domains in the MPB-composition PMN-32%PT to external stress, in comparison with the other two off-MPB compositions under the same polishing condition.

3.4.2. Mechanisms of local piezoelectric/ferroelectric responses changes

The MPB-composition, PMN-32%PT, is the easiest to be electrically switched by external dc voltages and has the strongest piezoelectric/ferroelectric responses, compared with the other two off-MPB compositions. The M phases in relaxor-PT crystals help to form the MPBs with R or T phases, resulting in phase instability, and inducing high piezoelectric response [9]. Electric-field-driven polarization rotation [32], the relatively lower energy barrier of the MPB-composition by Landau theory (Fig. 6a) and the strong piezoelectric anisotropy of the monoclinic distortion [43] contribute to these properties.

From another aspect, domain and domain wall related issues can be extrinsic factors contributing to the reported performances, ascribed to the minimization of depolarization field energy and elastic energy originated from the occurrence of multidomains in ferroelectrics [44]. These factors contain amount, shapes and sizes of domains, and the kinds and density of domain walls, together with domain wall motion. First of all, due to the property divergences in c^+ and c^- domains, large amount of c^+ domains and high aspect ratio of c^+/c^- in PMN-32%PT give rise to its small local V_c, resulting in the most easily excited domain wall motion under low external electric field. This high domain wall mobility facilities ease of polarization rotation [9], and thus contributes extrinsically to the better dielectric and piezoelectric performances. Besides, domain size is a key factor affecting local properties by influencing local depolarization and elastic energies. On the whole, both the formation of domains and domain walls decreases crystals' local elastic energy. Theoretically, the decrease in domain size gives rise to a decrease of depolarization and elastic energies. However, by domain size's decrease, the consequent requirement of domain wall increase (in amount/area/length) would lead to energy cost increase [45]. Hence, the determination of domain size is a balance of energies between domains and domain walls [45]. Fig. 6c-e illustrates the statistical analyses of vertical domain sizes in the three single crystals. Their raw domain partition and statistically analyses of area/length/width are present in Fig. S8-S10. Typically, domain width is commonly used for domain size description. Fig. 6e illustrates that the domain width in PMN-32%PT and PMN-40%PT are the largest and smallest, respectively. Similar trend can be seen in the single c^+ domain area from Fig. 6c. Among the three crystals, the largest single domain width/size in PMN-32%PT theoretically suggests its highest depolarization and elastic energies. These high energies makes domains in PMN-32%PT unstable and sensitive to external stress, evidenced by its small V_c, ease of electrical switching and the coupling of domain patterns with surface topographies. However, compared with those in PMN-24%PT, domains in PMN-40%PT with smaller width/sizes show electrical instability. This instability of these slim domains is a result of competition between domain and domain wall energies. In PMN-40%PT, the smaller domain width/size gives rise to lower depolarization and elastic energies, but the consequent larger domain wall amount causes energies increase. In the end these energies stemmed from domain and domain walls in PMN-40%PT are a little higher than those in PMN-24%PT, inducing smaller V_c and easier domain wall mobility. It is reasonable that PMN-32%PT with the largest domain width own the smallest coercive voltage, because the coercive field has been reported to have no certain relationships with domain size. For instance, it was found that in the [111]-oriented tetragonal PIN-PMN-PT crystals with domain sizes of 50 μm and 500 nm, the coercive field was almost the same, being 8.6 kV cm^{-1} [46]. This experimental result supports that the coercive field can be insensitive to the domain size. In addition, differences in curvature, width, types of domains walls in the crystals may cause energy differences and thus bring in performance variations. A clearer comparison of domain wall configuration and density on 1 μm × 1 μm in the crystals is present in Fig. S11.

Overall, the local piezoelectric responses are contributed by two factors, intrinsic one and extrinsic one. The intrinsic contribution is lattice deformation and energy barriers originated from symmetry differences, while the extrinsic one is related to domains and domain walls, such as aspect ratio of c^+/c^-, domain width/size, motion and density of domain walls. It alters from case to case and is still under debate whether the intrinsic or the extrinsic factor is in dominant contribution to the giant electromechanical responses in relaxor-PT solid solutions. By investigating the sub-coercive field piezoelectric behavior of PMN-PT crystals via the Rayleigh approach [43,47], it has been found that the irreversible contribution (representing the extrinsic contribution) is generally about 10%–20% for either R or M crystals [43], demonstrating that the intrinsic contribution (lattice) is mainly responsible for the high piezoelectric response. While, the contributions of PNRs to the shear piezoelectricity can be as much as 50%–80% [10]. In this work, we infer that the main factor could be the intrinsic one, although domains and domain walls do affect the local electromechanical responses to some extent.

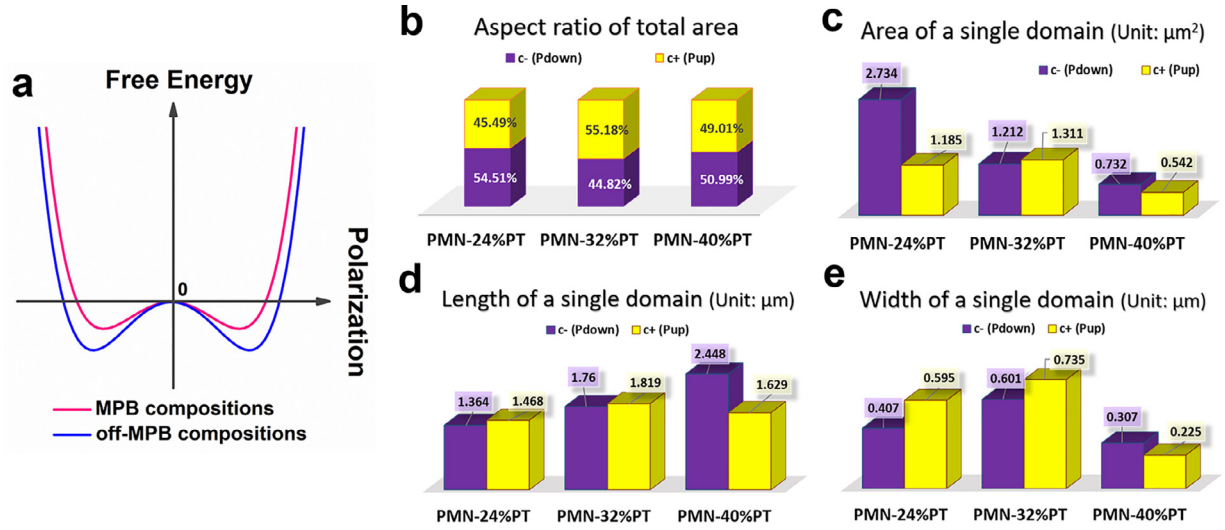

Fig. 6. (a) The schematic of free energy versus polarization in the at-MPB composition (PMN-32%PT) and the off-MPB compositions (PMN-24%PT and PMN-40%PT). (b-e) Statistical analyses of vertical domain sizes: (b) aspect ratio of total area; (c) area, (d) length, and (e) width of a single domain.

4. Conclusions

In this work, we quantitatively analyze the original local elastic/piezoelectric/ferroelectric properties of the various distinct symmetry-dependent vertical and lateral domain configurations in (100)-oriented PMN-x%PT single crystals via SPM, offering structure-property clarification from the aspect from microstructures. On mesoscale, with increasing contents of Ti^{4+} across MPB, labyrinthine domains with curved c/a walls change to polygonal lamellar ones with coexistence of relatively straight c, a and c/a walls, then to ribbon-like slim ones with c walls in small curvature. Among them, the polygonal lamellar domains in at-MPB composition with M symmetry, exhibit better performances: high effective Young's modulus, strong original average piezo response (8.5 pm) and effective d_{33} (14 pm V^{-1}), low coercive voltage, and ease of electrical switching. Balance between random field and ferroelectric interaction of nanoclusters, and gradient-driven morphological transition account for these domain formation. Low energy barrier in MPB-composition and strong piezoelectric anisotropy in monoclinic distortion contribute intrinsically to the attractive capabilities in PMN-32%PT. Higher and easier domain wall mobility, larger ratio of c^+/c^- domains, and larger depolarization and elastic energies originated from domains and domain walls make extrinsic contributions.

Declaration of Competing Interest

The authors declare no conflict of interest.

CRediT authorship contribution statement

Jihong Bian: Conceptualization, Methodology, Visualization, Investigation, Writing - original draft, Writing - review & editing, Project administration. **Pan Xue:** Software. **Ren Zhu:** Methodology. **Lei Wang:** Investigation. **Bian Yang:** Investigation. **Tao Li:** Writing - review & editing. **Qingyuan Hu:** Writing - review & editing. **Lvkang Shen:** Investigation. **Jianwei Wang:** Writing - review & editing. **Guanghao Lu:** Supervision, Writing - review & editing. **Yaodong Yang:** Supervision, Funding acquisition, Writing - review & editing.

Acknowledgments

This work was supported by the National Key R&D Program of China (2017YFA0208000), National Natural Science Foundation of China (Grant No. 51831010, 51621063), Program for Changjiang Scholars and Innovative Research Team in University (IRT_17R85) and the Fundamental Research Funds for the Central Universities (xtr0118016).

Supplementary material

Supplementary material associated with this article can be found, in the online version, at doi:10.1016/j.apmt.2020.100789.

Appendix A. Supplementary data

Supplementary data related to this article (The schematic of PMN-PT system's phase diagram, additional vertical domain configurations over larger/smaller scanning regions and responses the various dc tip-applied external electric fields by PFM, in-situ PFM domain retention results, additional AM-FM results) can be found online.

References

[1] I. Grinberg, D.V. West, M. Torres, G. Gou, D.M. Stein, L. Wu, G. Chen, E.M. Gallo, A.R. Akbashev, P.K. Davies, J.E. Spanier, A.M. Rappe, Perovskite oxides for visible-light-absorbing ferroelectric and photovoltaic materials, Nature 503 (2013) 509–512.
[2] P. Zhao, H. Wang, L. Wu, L. Chen, Z. Cai, L. Li, X. Wang, High-performance relaxor ferroelectric materials for energy storage applications, Adv. Energy Mater 9 (2019) 1803048.
[3] C. Qiu, B. Wang, N. Zhang, S. Zhang, J. Liu, D. Walker, Y. Wang, H. Tian, T.R. Shrout, Z. Xu, L.-.Q. Chen, F. Li, Transparent ferroelectric crystals with ultrahigh piezoelectricity, Nature 577 (2020) 350–354.
[4] F. Li, S. Zhang, T. Yang, Z. Xu, N. Zhang, G. Liu, J. Wang, J. Wang, Z. Cheng, Z.-.G. Ye, J. Luo, T.R. Shrout, L.-.Q. Chen, The origin of ultrahigh piezoelectricity in relaxor-ferroelectric solid solution crystals, Nat. Commun 7 (2016) 13807.
[5] F. Li, M.J. Cabral, B. Xu, Z. Cheng, E.C. Dickey, J.M. LeBeau, J. Wang, J. Luo, S. Taylor, W. Hackenberger, L. Bellaiche, Z. Xu, L.-.Q. Chen, T.R. Shrout, S. Zhang, Giant piezoelectricity of Sm-doped $Pb(Mg_{1/3}Nb_{2/3})O_3$-$PbTiO_3$ Single Crystals, Science 364 (2019) 264–268.
[6] V.V. Shvartsman, A.L. Kholkin, Domain structure of $0.8Pb(Mg_{1/3}Nb_{2/3})O_3$-$0.2PbTiO_3$ studied by piezoresponse force microscopy, Phys. Rev. B 69 (2004) 014102.
[7] X. Zhao, J.Y. Dai, J. Wang, H.L.W. Chan, C.L. Choy, X.M. Wan, H.S. Luo, Relaxor ferroelectric characteristics and temperature-dependent domain structure in a (110)-cut $(PbMg_{1/3}Nb_{2/3}O_3)0.75(PbTiO_3)_{0.25}$ single crystal, Phys. Rev. B 72 (2005) 064114.

[8] H. Fu, R.E. Cohen, Polarization rotation mechanism for ultrahigh electromechanical response in single-crystal piezoelectrics, Nature 403 (2000) 281–283.

[9] M. Davis, Picturing the elephant: giant piezoelectric activity and the monoclinic phases of relaxor-ferroelectric single crystals, J. Electroceram. 19 (2007) 25–47.

[10] F. Li, S. Zhang, Z. Xu, L.-.Q. Chen, The contributions of polar nanoregions to the dielectric and piezoelectric responses in domain-engineered relaxor-$PbTiO_3$ crystals, Adv. Funct. Mater. 27 (2017) 1700310.

[11] R.K. Vasudevan, Y. Cao, N. Laanait, A. Ievlev, L. Li, J.C. Yang, Y.H. Chu, L.Q. Chen, S.V. Kalinin, P. Maksymovych, Field enhancement of electronic conductance at ferroelectric domain walls, Nat. Commun. 8 (2017) 1318.

[12] N. Balke, B. Winchester, W. Ren, Y.H. Chu, A.N. Morozovska, E.A. Eliseev, M. Huijben, R.K. Vasudevan, P. Maksymovych, J. Britson, S. Jesse, I. Kornev, R. Ramesh, L. Bellaiche, L.Q. Chen, S.V. Kalinin, Enhanced electric conductivity at ferroelectric vortex cores in $BiFeO_3$, Nat. Phys. 8 (2011) 81–88.

[13] W.-.Y. Chang, C.-.C. Chung, C. Luo, T. Kim, Y. Yamashita, J.L. Jones, X. Jiang, Dielectric and piezoelectric properties of $0.7Pb(Mg_{1/3}Nb_{2/3})O_3$-$0.3PbTiO_3$ single crystal poled using alternating current, Mater. Res. Lett. 6 (2018) 537–544.

[14] Z.G. Ye, M. Dong, Morphotropic domain structures and phase transitions in relaxor-based piezo-/ferroelectric $(1-x)Pb(Mg_{1/3}Nb_{2/3})O_3$-$xPbTiO_3$ single crystals, J. Appl. Phys. 87 (2000) 2312–2319.

[15] F. Bai, J. Li, D. Viehland, Domain hierarchy in annealed (001)-oriented $Pb(Mg_{1/3}Nb_{2/3})O_3$-x%$PbTiO_3$ single crystals, Appl. Phys. Lett. 85 (2004) 2313–2315.

[16] M. Otonicar, H. Ursic, M. Dragomir, A. Bradesko, G. Esteves, J.L. Jones, A. Bencan, B. Malic, T. Rojac, Multiscale field-induced structure of $(1-x)Pb(Mg_{1/3}Nb_{2/3})O_3$-$xPbTiO_3$ ceramics from combined techniques, Acta Mater. 154 (2018) 14–24.

[17] T. Li, Z. Du, N. Tamura, M. Ye, S. Inguva, W. Lu, X. Zeng, S. Ke, H. Huang, Ferroelastic domain structure and phase transition in single-crystalline $[PbZn_{1/3}Nb_{2/3}O_3]_{1-x}[PbTiO_3]_x$ observed via in situ x-ray microbeam, J. Eur. Ceram. Soc. 38 (2018) 1488–1497.

[18] A.D. Ushakov, A.A. Esin, D.S. Chezganov, A.P. Turygin, A.R. Akhmatkhanov, Q. Hu, L. Sun, X. Wei, V.Y. Shur, In situ visualization of domain structure evolution during field cooling in 0.67PMN-0.33PT single crystal, IOP Conf. Ser.: Mater. Sci. Eng. 256 (2017) 012025.

[19] H.R. Zeng, H.F. Yu, R.Q. Chu, G.R. Li, H.S. Luo, Q.R. Yin, Domain orientation imaging of PMN–PT single crystals by vertical and lateral piezoresponse force microscopy, J. Cryst. Growth 267 (2004) 194–198.

[20] K. Fang, W. Jing, F. Fang, Multi-scale domain structure observation and piezoelectric responses for [001]-oriented PMN-33PT single crystal, J. Am. Ceram. Soc. 102 (2019) 7710–7719.

[21] D. Viehland, J. Li, E.V. Colla, Domain structure changes in $(1-x)Pb(Mg_{1/3}Nb_{2/3})O_3$-$xPbTiO_3$ with composition, dc bias, and ac field, J. Appl. Phys. 96 (2004) 3379–3381.

[22] A. Kholkin, A. Morozovska, D. Kiselev, I. Bdikin, B. Rodriguez, P. Wu, A. Bokov, Z.-.G. Ye, B. Dkhil, L.-.Q. Chen, M. Kosec, S.V. Kalinin, Surface domain structures and mesoscopic phase transition in relaxor ferroelectrics, Adv. Funct. Mater. 21 (2011) 1977–1987.

[23] Y. Liu, J. Xia, P. Finkel, S.D. Moss, X. Liao, J.M. Cairney, Real-time observation of stress-induced domain evolution in a [011] PIN-PMN-PT relaxor ferroelectric single crystal, Acta Mater. 175 (2019) 436–444.

[24] Q. Li, Y. Liu, R.L. Withers, Y. Wan, Z. Li, Z. Xu, Piezoresponse force microscopy studies on the domain structures and local switching behavior of $Pb(In_{1/2}Nb_{1/2})O_3$-$Pb(Mg_{1/3}Nb_{2/3})O_3$-$PbTiO_3$ single crystals, J. Appl. Phys. 112 (2012) 052006.

[25] W. He, T. Jiang, Q. Li, X. Xi, Q. Yan, Anisotropic domain structures of $Pb(Mg_{1/3}Nb_{2/3})O_3$-$PbZrO_3$-$PbTiO_3$ single crystals with high ferroelectric phase transition temperature, J. Am. Ceram. Soc. 100 (2017) 1724–1732.

[26] W. He, Q. Li, Y. Sun, X. Xi, Y. Zhang, Q. Yan, Investigation of piezoelectric property and nanodomain structures for PIN-PZ-PMN-PT single crystals as a function of crystallographic orientation and temperature, J. Mater. Chem. C 5 (2017) 2459–2465.

[27] R.-.X. Wang, J. Zhang, L.-.M. Zheng, L. Sun, Z.-.L. Luo, S.-.T. Zhang, B. Yang, Evolution of polar nano-regions under electric field around ferro-paraelectric transition temperature and its contribution to piezoelectric property in $Pb(Mg_{1/3}Nb_{2/3})O_3$-$0.30PbTiO_3$ crystal, Ceram. Int. 44 (2018) 18084–18089.

[28] M.F. Wong, K. Zeng, Elastic-plastic deformation of $Pb(Zn_{1/3}Nb_{2/3})O_3$-(6-7)%$PbTiO_3$ single crystals during nanoindentation, Philos. Mag 90 (2010) 1685–1700.

[29] M.F. Wong, K. Zeng, Nanoscale domains and preferred cracking planes in $Pb(Zn_{1/3}Nb_{2/3})O_3$-(6-7)%$PbTiO_3$ single crystals studied by piezoresponse force microscopy and fractography, J. Appl. Phys. 107 (2010) 124104.

[30] R. Keech, L. Ye, J.L. Bosse, G. Esteves, J. Guerrier, J.L. Jones, M.A. Kuroda, B.D. Huey, S. Trolier-McKinstry, Declamped piezoelectric coefficients in patterned 70/30 lead magnesium niobate-lead titanate thin films, Adv. Funct. Mater. 27 (2017) 1605014.

[31] M.J. Krogstad, P.M. Gehring, S. Rosenkranz, R. Osborn, F. Ye, Y. Liu, J.P.C. Ruff, W. Chen, J.M. Wozniak, H. Luo, O. Chmaissem, Z.G. Ye, D. Phelan, The relation of local order to material properties in relaxor ferroelectrics, Nat. Mater. 17 (2018) 718–724.

[32] H. Liu, J. Chen, L.L. Fan, Y. Ren, L. Hu, F.M. Guo, J.X. Deng, X.R. Xing, Structural evidence for strong coupling between polarization rotation and lattice strain in monoclinic relaxor ferroelectrics, Chem. Mater. 29 (2017) 5767–5771.

[33] Z. Zhang, J. Xu, L. Yang, S. Liu, J. Xiao, R. Zhu, X. Li, X.a Wang, H Luo, The performance enhancement and temperature dependence of piezoelectric properties for $Pb(Mg_{1/3}Nb_{2/3})O_3$-$0.30PbTiO_3$ single crystal by alternating current polarization, J. Appl. Phys. 125 (2019) 034104.

[34] B. Akkopru-Akgun, W. Zhu, M.T. Lanagan, S. Trolier-McKinstry, The effect of imprint on remanent piezoelectric properties and ferroelectric aging of $PbZr_{0.52}Ti_{0.48}O_3$ thin films, J. Am. Ceram. Soc. 102 (2019) 5328–5341.

[35] W.-.H. Kim, J.Y. Son, Y.-.H. Shin, H.M. Jang, Imprint control of nonvolatile shape memory with asymmetric ferroelectric multilayers, Chem. Mater. 26 (2014) 6911–6914.

[36] W.-.Y. Chang, C.-.C. Chung, Z. Yuan, C.-.H. Chang, J. Tian, D. Viehland, J.-.F. Li, J.L. Jones, X. Jiang, Patterned nano-domains in PMN-PT single crystals, Acta Mater. 143 (2018) 166–173.

[37] Y. Zhou, Q. Li, C. Xu, F. Zhuo, Q. Yan, Y. Zhang, X. Chu, Anisotropic domain switching in $Pb(Mg_{1/3}Nb_{2/3})O_3$-$0.30PbTiO_3$ single crystals with rhombohedral structure, J. Am. Ceram. Soc. 101 (2018) 3054–3064.

[38] V.V. Shvartsman, A.L. Kholkin, Polar structures of $PbMg_{1/3}Nb_{2/3}O_3$-$PbTiO_3$ relaxors: piezoresponse force microscopy approach, J. Adv. Dielectr. 02 (2012) 1241003.

[39] E.A. Eliseev, Y.M. Fomichov, S.V. Kalinin, Y.M. Vysochanskii, P. Maksymovich, A.N. Morozovska, Labyrinthine domains in ferroelectric nanoparticles: manifestation of a gradient-induced morphological transition, Phys. Rev. B 98 (2018) 054101.

[40] M.F. Wong, K. Zeng, Mechanical polishing effects toward surface domain evolution in $Pb(Zn_{1/3}Nb_{2/3})O_3$-$PbTiO_3$ single crystals, J. Am. Ceram. Soc. 94 (2011) 1079–1086.

[41] H.D. Lu, S. Liu, Z.Y. Ye, S. Yasui, H. Funakubo, A.M. Rappe, A. Gruverman, Asymmetry in mechanical polarization switching, Appl. Phys. Lett. 110 (2017) 222903.

[42] Y. Zhang, H. Lu, L. Xie, X. Yan, T.R. Paudel, J. Kim, X. Cheng, H. Wang, C. Heikes, L. Li, M. Xu, D.G. Schlom, L.-.Q. Chen, R. Wu, E.Y. Tsymbal, A. Gruverman, X. Pan, Anisotropic polarization-induced conductance at a ferroelectric–insulator interface, Nat. Nanotechnol. 13 (2018) 1132–1136.

[43] S. Zhang, F. Li, High performance ferroelectric relaxor-$PbTiO_3$ single crystals: status and perspective, J. Appl. Phys. 111 (2012) 031301.

[44] A.N. Morozovska, E.A. Eliseev, I.S. Vorotiahin, M.V. Silibin, S.V. Kalinin, N.V. Morozovsky, Control of polarization reversal temperature behavior by surface screening in thin ferroelectric films, Acta Mater. 160 (2018) 57–71.

[45] G. Catalan, J. Seidel, R. Ramesh, J.F. Scott, Domain wall nanoelectronics, Rev. Mod. Phys. 84 (2012) 119–156.

[46] D. Lin, S. Zhang, Z. Li, F. Li, Z. Xu, S. Wada, J. Luo, T.R. Shrout, Domain size engineering in tetragonal $Pb(In_{1/2}Nb_{1/2})O_3$-$Pb(Mg_{1/3}Nb_{2/3})O_3$-$PbTiO_3$ crystals, J. Appl. Phys. 110 (2011) 084110.

[47] M. Dietze, H. Katzke, M. Es-Souni, N. Neumann, H.-.S. Luo, Single domain vs. polydomain [111] $0.72Pb(Mg_{1/3}Nb_{2/3})O_3$-$0.28PbTiO_3$ single crystal. Polarization switching, dielectric and pyroelectric properties, Appl. Phys. Lett. 100 (2012) 242905.